SUPPLEMENTARY

Whole-brain calcium imaging during physiological vestibular stimulation in larval zebrafish

Geoffrey Migault[1,2], Thomas Panier[1,2], Raphaël Candelier[1,2], Georges Debrégeas[1,2], Volker Bormuth*[1,2]

[1]Sorbonne Université, UMR 8237, Laboratoire Jean Perrin, F-75005 Paris, France.

[2]CNRS UMR 8237, Laboratoire Jean Perrin, F-75005 Paris, France.

*corresponding Author

Content

The setup

The miniaturized digital scanning light-sheet forming unit

A laser beam (488nm) is delivered via a single mode optical fiber, onto the rotating platform where it is collimated with an objective (5x NA 0.16), projected onto a galvanometric mirror and then focused into the specimen with a second objective (5x NA 0.16) (Figure S1). A function generator drives the mirror to oscillate at 400Hz resulting in a quasi-parallel displacement of the laser in the imaging plane and the formation of a thin sheet of light. Volumetric scanning is obtained by moving the fiber outlet with a piezo actuator resulting in a parallel translation of the light-sheet in the z-direction. The dimension of the light-sheet forming unit is 9x6x10cm. The objectives, the galvanometric mirror and the piezo actuator are fixed onto a custom machined metal block. No further alignment of these elements is necessary. For alignment of the light-sheet relative to the objective focal plane, the light-sheet unit can be rotated and translated in 4 degrees of freedom. This simplifies the alignment procedure as no mirrors or lenses move relative to each other.

Design and theoretical description of the laser path

In laser scanning microscopy, the scanning mirror is positioned such that its pivoting point is conjugated of the back focal plane of the objective. In this configuration, the objective transforms the angular motion of the laser introduced by the mirror into a parallel displacement of the laser beam perpendicular to the optical axis. As the back focal plane lies inside the objective, a telescope (relay lenses) is generally needed between the scanning mirror and the objective to optically conjugate the pivoting point of the mirror with the back focal plane. This requirement yields relatively long optical pathways between the light source and the specimen in digital scanning light-sheet microscopy.
Here we show that this requirement can in fact be relaxed without precluding the optical performances of the microscope. The scanning mirror is located immediately behind the illumination objective, at a distance Δx away from the back focal plane (Figure S1a). In this configuration, the mirror rotation laterally displaces the laser beam but also introduces a tilting of the beam relative to the optical axis by an angle $\alpha = \arctan(\Delta x * y / f^2)$, where y *is* the scan distance relative to the optical axis and f is the focal length of the objective. At the border of the field of view, y = 250µm; with f = *33*mm and Δx = 1.5cm, this yields an angle α=0.16° that is only 1.2% of the divergence angle of the laser beam β = 2 * arcsin(NA/n) = 13.78° with the numerical aperture NA = 0.16 and the refractive index of water n = 1.33. This minute variation in the beam orientation has in practice no significant effect on the quality of the light-sheet.
We performed a similar calculation for the z-scan. Instead of using a second mirror, we move the fiber outlet (Figure S1b). The collimation objective transforms the parallel movement of the fiber outlet into a rotation of the laser beam around the focal point of the collimation objective. Δx is now defined as the distance between the focal points of the two objectives, which is minimized but large enough to accommodate the scanning mirror. At the extremity of the sample z = 100 µm and with f = 33mm and Δx = 3cm the angle α is again only 1.2% of the divergence angle of the laser. This corresponds to a displacement of the light-sheet relative to the focal plane of less than 1.2 % of the light-sheet thickness.

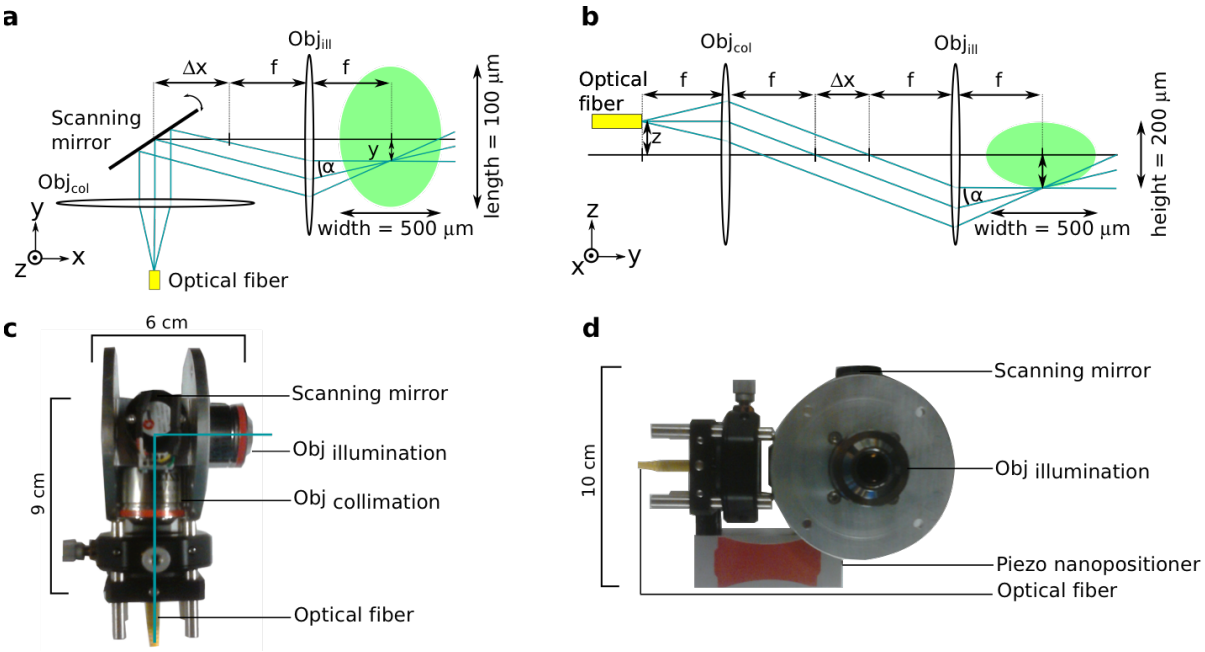

Figure S1 | Ray diagram of the light-sheet unit. (a) Top view illustrating the scanning mechanism for the light-sheet formation. (b) Side view illustrating the ray diagram for the z-scanning of the light-sheet. Note that the scanning mirror is omitted for clarity. The green ellipse schematizes the fluorescent zebrafish brain. (c) Top view of the light-sheet forming unit. (d) Side view of the light-sheet forming unit. The two metallic disks allow to rotate the unit for alignment.

Sample holder and sample preparation

Larvae are placed into 2% low melting point agarose and then drawn into a glass capillary tube with 1mm inner diameter. After gelification, the larva is partially extruded and the agarose is removed around the eyes. The capillary tube is then introduced into the microscope, hold by a x-z translation stage and supported mechanically by a plastic cylinder with O-rings on both sides to make the system water proof (Figure S2). For imaging the agarose cylinder is partially extruded from the capillary and positioned in the detection plane of the light-sheet microscope.

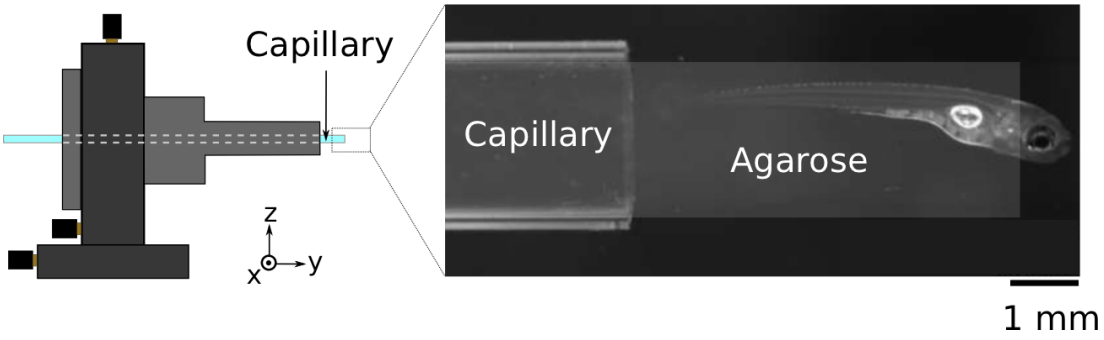

Figure S2 | Sample holder and sample preparation.

The fluorescence detection unit

The fluorescence detection unit comprises a 20x water immersion objective (NA = 1) attached to a piezo actuator for volumetric imaging (closed loop travel range 250µm) and mounted on a manual translation stage to adjust the focal plane with the light-sheet plane. Before rotating the microscope, the translation stage is blocked with fixation screws to prevent movements during rotation. A notch filter (488nm) and a low-pass filter (950nm blocking edge) are used to block the photons from the excitation laser and from the infrared light used for behavioral monitoring. The image is projected via a GFP-filter and a tube lens (f = 150mm) onto a fast sCMOS camera (Hamamatsu, V2). To reduce the camera weight Hamamatsu removed for us the camera water cooling unit that is not used during fast light-sheet microscopy.

Parts list of the setup

	Element	Characteristics	Reference	Company
Light-sheet unit	Laser	488nm	LBX-488-50-CSB-PP	Oxxius, France
	Optical fiber	Single mode	P1-460-FC-2	Thorlabs
	Breadboard	45 x 30 cm	MB3045/M	Thorlabs
	Collimation objective	NA 0.16, 5x	Plan-Neofluar 5x/0.16	Zeiss
	Illumination objective	NA 0.16, 5x	Plan-Neofluar 5x/0.16	Zeiss
	Galvano mirror		Model: TSH8203 S/N TSH22700-Y	Century Sunny
	Function generator		33220A	Agilent
	z-piezo nanopositioner		PZ 400 SG OEM	Piezo Jena
Detection unit	Objective	NA 1.0, 20x	XLUMPLFLN20x	Olympus
	Tube lens	f = 150 mm	AC254-150-A	Thorlabs
	Notch filter	488nm	NF488-15	Thorlabs
	GFP filter	525 nm	MF525-39	Thorlabs
	Low pass filter	950nm blocking edge	FF01-750/SP-25	Semrock
	Camera	sCMOS, lightweight	V2	Hamamatsu
	PIFOC		P-725.2CD	Physical Instruments
Data acquisition	Acquisition board		NI PCIe-6363	National Instruments
Behavior tracking unit	Camera		FLU-U3-13Y3M-C	Point Grey
	Objective		1-61449	Navitar
	2x Adapter		1-61450	Navitar
	Infra-red LED	850 nm	SFH 4740	Osram
Other elements	Motor		ALAR150SP	Aerotech
	controller		SOLOISTCP30-MXU	Aerotech

Table 1 | Parts list of the setup

Setup characterization

Light-sheet profile

While keeping fixed the detection objective, we performed a z-sweep of the light-sheet through a sample holding 100nm in diameter fluorescent beads (FluoSpheres,505/515, Molecular Probes, USA) embedded in 2% low melting point agarose. The spacing between consecutively imaged sections was 0.5 μm. We extracted the local thickness of the light sheet (half width at $1/e^2$) by fitting the measured fluorescent profile along the z-direction with a Gaussian function (Matlab). The result is shown in Figure S3 as a function of the bead position along the laser beam propagation direction. The light-sheet thickness is consistent with the theoretical description of a Gaussian beam

$$\omega(x) = \omega_0 \sqrt{1 + \left(\frac{\lambda x}{\pi \omega_0}\right)^2}$$

with the laser beam wavelength λ and the beam profile waist at $1/e^2$ of $\omega_0 = 2.04 \pm 0.02$ μm (std).

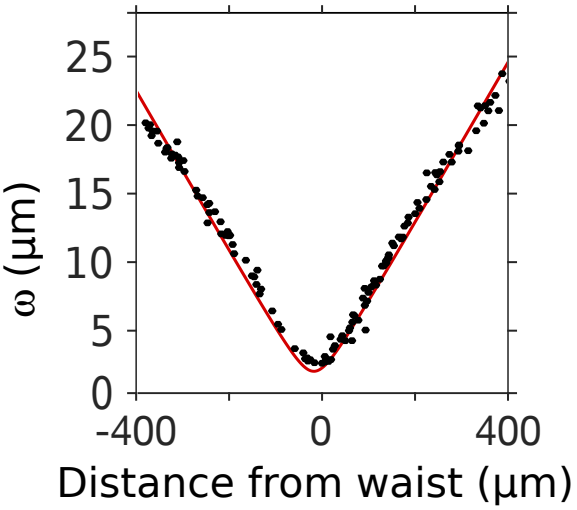

Figure S3 | Light-sheet profile. Measured light-sheet profile (black) and fit with theoretical description of a Gaussian beam profile (red).

Mechanical stability of the scanned volume during microscope rotation

To characterize the stability of our setup, we took advantage of a 3D tracking method of microspheres that enables nm resolution at low magnifications[3]. With our light-sheet system we imaged fluorescent microspheres of 1μm in diameter (ThermoFisher Scientific, USA) embedded in agarose. The image of a microsphere displaced relative to the focal plane of the detection objective shows a characteristic interference pattern in the form of concentric rings (Figure S4a). The diameter of these rings varies as a function of the displacement of the sphere relative to the focal plane. Figure S4b shows the radial intensity profile averaged over all angles as a function of the imposed objective height. This measurement serves as a look-up-table (LUT) to determine with nanometer precision the microsphere z-position relative to the objective focal plane during microscope rotation by fitting an instantaneous radiation profile onto this LUT. To test the procedure, we moved the objective in cycles of five steps of 0.5μm in the z-direction, acquired the corresponding interference pattern of the

microsphere image and finally inferred its z-position by fitting this profile onto the LUT. The mean of the measured z-position is shown in Figure S4c as a function of the imposed objective position. This method yields a tracking accuracy of 10nm (standard deviation, N = 5). In addition, the program determines with precision of less than 100 nm the x and y position of the sphere. With this method, we measure the relative 3D drift of the specimen with respect to the observation objective during rotation of the microscope (Figure S4d). Over the angular range, the in-plane and axial displacements are below 2µm and 500nm, respectively, and mostly reflect the finite stiffness of the piezo-crystal holding the detection objective.

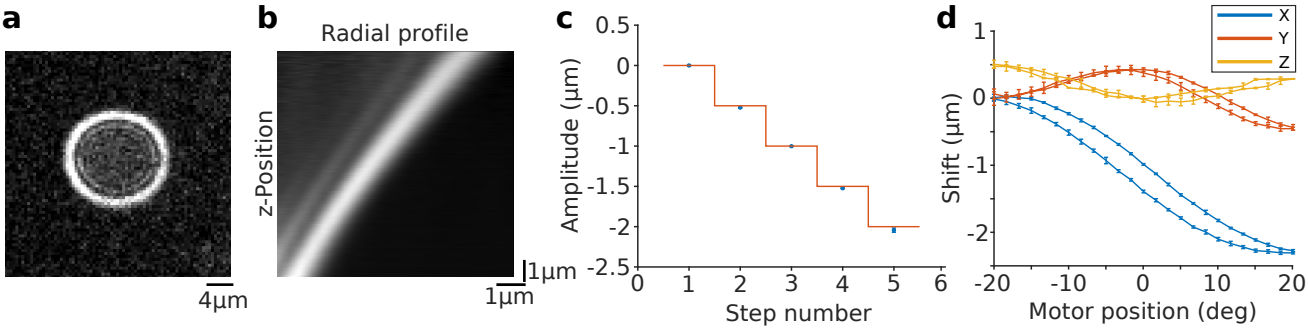

Figure S4 | Stability characterization with 3D tracking of microspheres. (a) Characteristic interference pattern of a fluorescent microsphere displaced relative to the focal plane of the detection objective. (b) Radial intensity profile averaged over all angles as a function of the imposed objective height. This profile serves as a look-up-table (LUT) to quantify z-movements of the microsphere during microscope rotation. (c) Control signal that drives a piezo to displace the detection objective in steps of 0.5µm (red) and the measured relative distance of the microsphere to the objective (blue, errorbars = std, N = 5) determined by fitting the instantaneous intensity profile of the microsphere onto the LUT shown in b. (d) 3D tracking of the microsphere position during a sinusoidal microscope rotation. Only a slide hysteresis is seen during a full cycle.

Rotating the microscope leads to minute movements of the specimen relative to the imaging plane. The in-plane displacements can be easily corrected during post-processing using successive image registration. In contrast, the axial drift cannot be compensated and may introduce artefactual modulations of the fluorescent signals. To quantify the noise level associated with these effects, we performed control experiments with paralyzed fish expressing a red fluorescent protein pan-neurally (HuC:RFP). We rotated the microscope in alternating positive and negative steps with 20s dwell time and of increasing amplitude from 5° to 25° with 5° increment and with peak velocity and peak acceleration of 60°/s and 10000°/s^2 respectively (Figure S5a). Simultaneously, we recorded brain stacks of 20 layers at 2.5Hz per volume. For each step, we estimated the mean intensity change per pixel induced by the rotation relative to the mean intensity value measured at zero-degree rotation before each step. We then performed the same analysis without rotation to estimate the intrinsic noise level of our recordings. Figure S5b shows for a -15° step the histogram of the pixel-wise measured intensity change in one image plane during microscope rotation (red) compared to the noise distribution under static conditions (pink). We estimate the noise level (Δ sigma) introduced by the microscope rotation as the difference of the standard deviations of both distributions as estimated by Gaussian fits. This mechanical-induced noise increases with the rotation amplitude, but remains below 2% ΔF/F (mean over 3 fish) over a range of ±25° (Figure S5c, red). In a second set of control experiments, we repeated the same analysis with paralyzed fish expressing the calcium reporter GCaMP6s pan-neurally (Figure S5b-c, blue). We estimated the distribution standard deviations for the static and for the dynamic case by Gaussian fits to the left side of the distributions and calculated

from the results the mechanical noise level Δ sigma (Figure S5c blue, mean over 3 fish). The measured mechanical noise level shows the same amplitude and trend as a function of increasing rotation angles compared to the measurement with the RFP fish and this even though GCaMP6s has a lower base fluorescence signal compared to RFP and spontaneous activity introduces extra noise. From these two measurements, we conclude that the mechanical noise level is less than 3% ΔF/F for a microscope rotation range of ±25°.

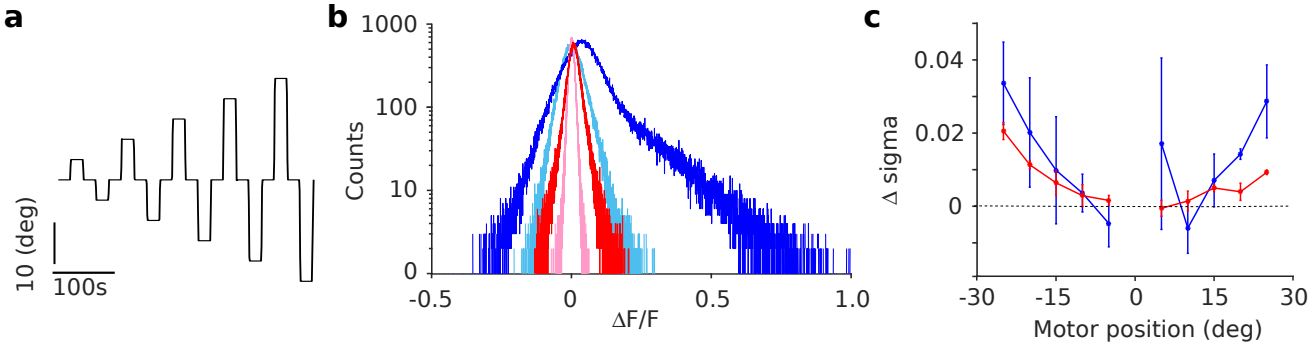

Figure S5 | Noise level. (a) Step stimulation protocol. (b) Histogram of the intensity change per pixel induced by a -15° microscope rotation relative to the intensity value measured just before the step (RFP (red) and GCamP6s (blue) expressing fish). Light colors correspond to the intrinsic noise level measure without microscope rotation. (c) Mean noise level measured with RFP (red) and with GCaMP6s (blue) expressing fish (error bars = std, N = 3 fish).

Data acquisition and analysis

Image acquisition, mirror scanning, objective motion and eye monitoring were synchronized using a D/A multifunction card (NI USB-6259 NCS, National Instruments) and a custom-written program in Matlab (The MathWorks) and in LabVIEW (National Instruments).

Sinusoidal stimulation (Figure 2)

Acquisition rate was set at 2.5 stacks per second (20 brain sections, 10µm inter-slice separation) and images were binned down to a pixel size of 0.8x0.8 μm^2. A typical recording lasted for 20min corresponding to 240 stimulation cycles.

For every voxel in the recorded 4D brain stack we calculated the power spectrum of the fluorescent time trace, estimated amplitude, A, and phase, φ, at the stimulation frequency and represented the phase map as hsv image stack (hue = phase, saturation = 0, value = amplitude). Every pixel in the phase map is described by a complex number $z=A*e^{i\varphi}$. To average phase maps obtained for different fish, we first registered with the Computational Morphometry ToolKit CMTK (http://www.nitrc.org/projects/cmtk/) the average fluorescent brain stack (anatomical stack) for every fish onto a unique reference brain. The reference brain was obtained by averaging four different samples (Tg*(elavl3:*GCaMP6f), 6 dpf) imaged with a standard light-sheet microscope at high spatial resolution (voxel size 0.8x0.8x2 µm). With the found rigid transformations we transformed the real and the imaginary part of the corresponding phase maps, averaged the transformed real and imaginary parts for different fish and finally calculated from the average complex number amplitude and phase of the average phase map $< z > = <a> + i<b> = <A> * e^{i <\varphi>}$. We further used CMTK to compute the morphing transformation from our reference brain to the Tg(*elavl3*:GCaMP5G) stack of

the Z-Brain atlas[2]. This allowed us to map the functional data onto the Z-Brain Viewer and thus to position various clusters relative to labeled anatomical landmarks in the reference brain.

To obtain the symmetric response map in Figure 2b we compared the amplitude of every pixel to its counterpart in the other brain hemisphere and replaced its amplitude value by the minimum of the two values. This procedure makes use of the bilateral symmetry of the vestibular circuit in order to eliminates spurious signal unrelated to the vestibular stimulation.

Note that the measured fluorescent response is shifted relative to the phase of the real neuronal signal due to the response function of the GCaMPs sensor $\Delta\varphi_{neuron} = \Delta\varphi_{measured} - \Delta\varphi_{GCaMP6s}$.

The response function of the GCaMP6s sensor can be approximated by an exponential function:

$$K(t) = \frac{1}{\tau} e^{-\frac{t}{\tau}}\ \theta(t) \qquad \text{(Eq. 1)}$$

with the time constant τ=2.6s [1] of the fluorescent decay of the GCaMP6s sensor and the step function $\theta(t)$.

The fluorescent response of the sensor is the convolution of the neuronal signal $n(t)$ with the GCaMP6s kernel:

$$F(t) = n(t) * K(t)$$

In the case of a sinusoidal neuronal response $n(t) = A\sin(\omega t)$ we find:

$$F(t) = -\frac{\omega\tau}{1+(\omega\tau)^2}\cos(\omega t) + \frac{1}{1+(\omega\tau)^2}\sin(\omega t) = A\sin(\omega t + \varphi_{GCaMP})$$

And with $\sin(\omega t + \varphi) = \sin(\varphi)\cos(\omega t) + \cos(\varphi)\sin(\omega t)$ and $\tan(\varphi) = \frac{\sin(\varphi)}{\cos(\varphi)}$
we can determine the phase shift as:

$$\varphi_{GCaMP6s} = \arctan(-\omega\tau) = \arctan(-2\pi f\tau) = -1.27 \text{ rad}$$

To illustrate the corresponding neuronal phase map in Figure 2d we added a second set of labels (ϕ_n) to the color map bar that was shifted by this uniform value relative to the set of labels corresponding to the fluorescent phase map (ϕ_f).

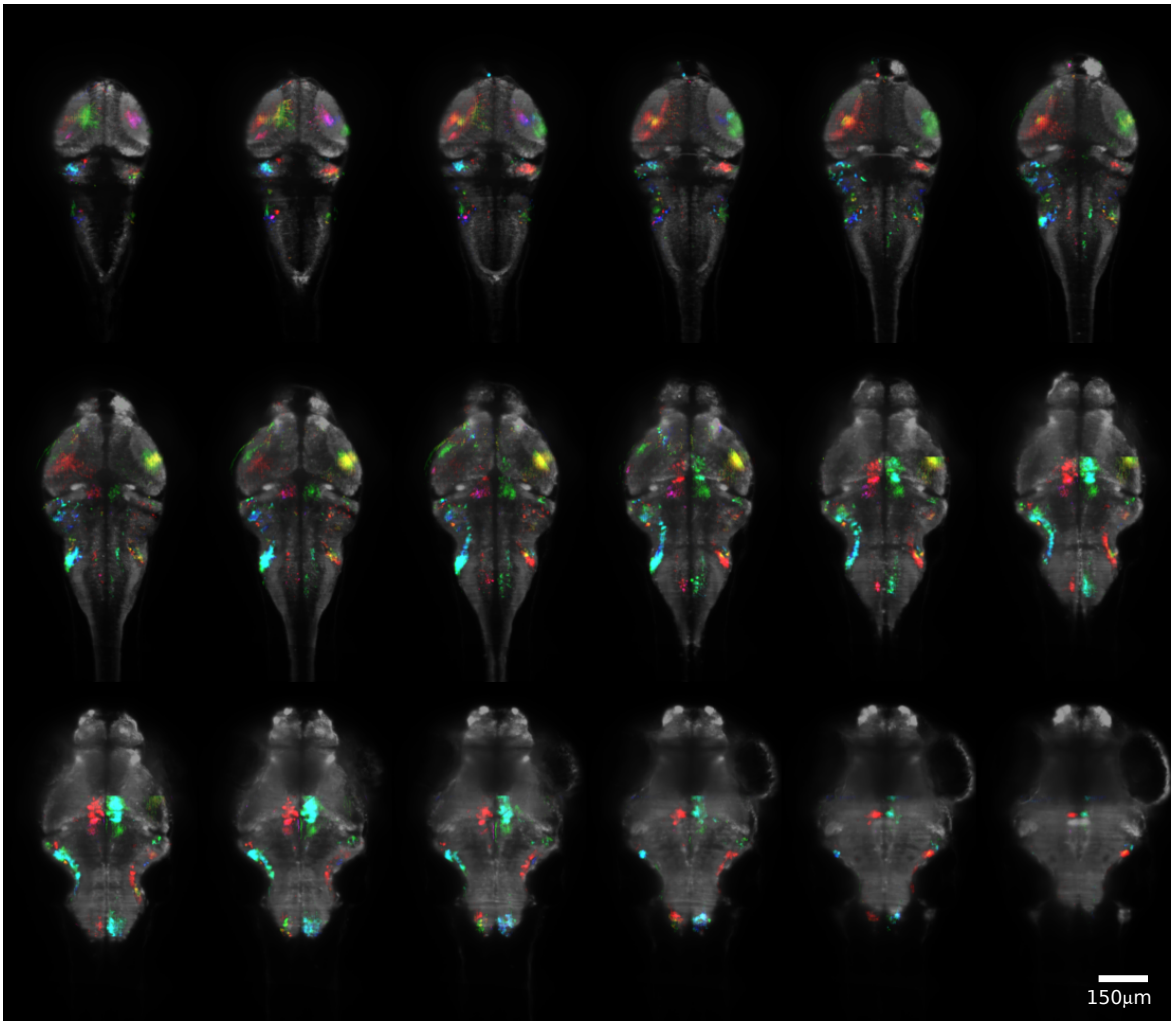

Figure S6 | Mean phase map. The mean phase map was calculated after the individual maps (N=3) where mapped onto a high-resolution reference brain. From the interpolated mean phase map, we extracted the shown 18 layers with 8µm inter-slice separation.

Figure S7 | Phase map in paralyzed fish. The image shows a Z-projection of the phase map.

Step stimulation (Figure 3)

Acquisition rate was set at 2.5 stacks per second (20 brain sections, 10 μm inter-slice separation) and images were binned down to a pixel size of 0.8x0.8 μm^2. Steps were controlled at maximal angular velocity of 30°/s in cycles of three steps with increasing amplitude (10°, 15°, 20°) and 10s dwell time. A typical recording lasted for 10 min corresponding to 10 stimulation cycles.

Supplementary Movies

Movie S1 | High-resolution volumetric brain scan.
6dpf old larval zebrafish with pan-neuronal GCaMP6s expression, 1μm inter-section separation.

Movie S2 | Functional brain-wide response to sinusoidal vestibular rolling stimulation.
Average over 120 cycles (2x accelerated). Shown are 4 out of 20 recorded sections. Bottom left: The rotating microscope. Bottom right: Front view of the zebrafish larva making compensatory eye movements in response to the vestibular rolling stimulus.
Stimulation parameters: 0.2Hz stimulation frequency, ±10° stimulation amplitude
Acquisition parameters: 2.5 stacks per second, 20 brain sections, 10μm inter-slice separation.

Movie S3 | Animated multi-angle view of the z-projection of the mean phase map.
We calculated for every perspective a z-projection. The dorsal view corresponds to the phase map shown in Figure 2d.

Movie S4 | Functional brain-wide response to vestibular rolling step stimulation.
Average over 10 stimulation cycles (12x accelerated). Shown are 4 out of 20 recorded sections. Bottom left: The rotating microscope. Bottom right: Front view of the zebrafish larva making compensatory eye movements in response to the vestibular rolling stimulus.
Stimulation parameters: 30°/s maximal angular velocity, 3 steps per cycle with 10°, 15° and 20° amplitude, 10s dwell time.
Acquisition parameters: 2.5 stacks per second, 20 brain sections, 10μm inter-slice separation.

References

1. Chen T-W, Wardill TJ, Sun Y, Pulver SR, Renninger SL, Baohan A, et al: Ultrasensitive fluorescent proteins for imaging neuronal activity. **Nature 499**:295–300, 2013
2. Randlett O, Wee CL, Naumann EA, Nnaemeka O, Schoppik D, Fitzgerald JE, et al: Whole-brain activity mapping onto a zebrafish brain atlas. **Nat Methods 12**:1039–1046, 2015
3. van Loenhout MTJ, Kerssemakers JWJ, De Vlaminck I, Dekker C: Non-bias-limited tracking of spherical particles, enabling nanometer resolution at low magnification. **Biophys J 102**:2362–2371, 2012